Revealing Extraordinary Intrinsic Tensile Plasticity in Gradient Nano-Grained Copper

T. H. Fang, *et al.*

Science **331**, 1587 (2011);
DOI: 10.1126/science.1200177

Revealing Extraordinary Intrinsic Tensile Plasticity in Gradient Nano-Grained Copper

T. H. Fang,* W. L. Li,* N. R. Tao,* K. Lu†

Nano-grained (NG) metals are believed to be strong but intrinsically brittle: Free-standing NG metals usually exhibit a tensile uniform elongation of a few percent. When a NG copper film is confined by a coarse-grained (CG) copper substrate with a gradient grain-size transition, tensile plasticity can be achieved in the NG film where strain localization is suppressed. The gradient NG film exhibits a 10 times higher yield strength and a tensile plasticity comparable to that of the CG substrate and can sustain a tensile true strain exceeding 100% without cracking. A mechanically driven grain boundary migration process with a substantial concomitant grain growth dominates plastic deformation of the gradient NG structure. The extraordinary intrinsic plasticity of gradient NG structures offers their potential for use as advanced coatings of bulk materials.

Extensive investigations over the past few decades indicated that with a substantial reduction of grain sizes into the nanometer regime, the strength of polycrystalline metals is greatly increased at the expense of their ductility (*1*, *2*). Free-standing nano-grained (NG) metals usually exhibit a very high strength and a very limited tensile ductility (with a uniform elongation of few percent) and almost no work-hardening before catastrophic failure (*3*). The brittleness is believed to be an intrinsic "Achilles' heel" of NG metals because the conventional deformation mechanisms cease to operate: Dislocation slip is substantially suppressed by the extremely small grains (which accounts for the extreme strengthening in NG metals) and grain boundary (GB) sliding or diffusional creep is not active enough to accommodate plastic straining at ambient temperature (*3*).

Experimental observations hint that the observed brittleness in NG metals might be extrinsic rather than intrinsic. For instance, dimples have been observed in fracture surfaces of various NG metals, signifying substantial plastic deformation before failure (*4*, *5*). Large plastic strains can be obtained in other deformation modes such as compression and rolling (*6*, *7*). Indeed, limited tensile ductility of NG metals is often attributed to the absence of work-hardening of nano-sized grains, so that strain localization and early necking occur immediately after yielding. Thus, the intrinsic tensile plasticity may have not been revealed due to superimposition of the strain localization and early necking. Intrinsic tensile plasticity of NG samples might be detected provided the strain localization is effectively suppressed.

Previous studies (*8*, *9*) showed that confinement by a ductile substrate is effective in suppressing strain localization in NG metal films under tension. Tensile elongation of NG Cu films adherent on a polymer substrate can be enhanced up to 10% before failure through debonding of the film and substrates. A higher ductility is expected if the strain localization in the NG film could be better suppressed. The elastic mismatch and the interface bonding between the film and the matrix are two key parameters controlling the confinement. Consequently, an ideal architecture might be a NG element metal film adherent on a coarse-grained (CG) substrate of the same metal with a graded grain-size transition between them. This gradient architecture without a shape interface between the NG film and the CG substrate, which is elastically homogeneous but plastically gradient, may offer unusual mechanical responses (*10*) and provide a unique opportunity for revealing the intrinsic tensile plasticity of NG metals without strain localization.

For synthesizing such an architecture, surface nanocrystallization of CG metals by means of surface plastic deformation techniques (*11*, *12*) is a feasible option. Here, we have used a surface mechanical grinding treatment (SMGT) (*13*) for preparing a NG Cu film with a spatial gradient in grain size on a bulk CG Cu substrate and have achieved a large tensile plasticity in the NG structure and revealed a different governing deformation mechanism.

CG Cu dog-bone–shaped tensile bar specimens with a gauge diameter of 6 mm and gauge length of 20 mm were processed by means of SMGT at cryogenic temperature to form a NG surface layer in the gauge section (Fig. 1) (*14*). After treatment, the topmost layer of the specimens consists of nano-sized elongated grains with random crystallographic orientations (Fig. 1, D and E), with an average transversal grain size of about 20 nm and an aspect ratio of 2.0 (Fig. 1F). Transmission electron microscopy (TEM) measurements showed an increasing grain size gradually with an increasing depth. The average transversal grain sizes are <100 nm in the top 60-μm-thick layer and increase to about 300 nm in a depth of 60 to 150 μm. Below 150-μm depth are typical deformation structures in coarse grains, characterized by dislocation tangles or dislocation cells with sizes ranging from submicrometers to micrometers. The thickness of the deformed CG layer is about 500 to 700 μm. In the top 150-μm-thick layer, a gradient nano-grained (GNG) structure with grain sizes varying from 20 to 300 nm is formed on the CG substrate.

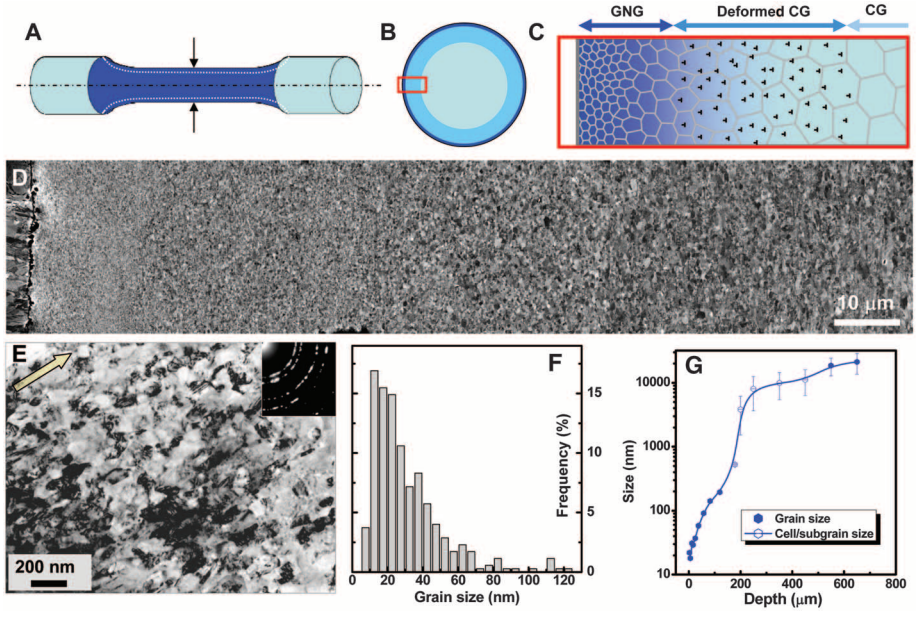

Fig. 1. (**A**) Schematic of the tensile bar sample of which the gauge section was processed by means of SMGT. (**B** and **C**) Schematic of the cross-sectional microstructure of the gauge consisting of a GNG layer (dark blue) and a deformed CG layer (blue) on a CG core (light blue). (**D**) A typical cross-sectional SEM image of a SMGT Cu sample. (**E**) A cross-sectional bright-field TEM image of microstructures 3 μm below the treated surface. The arrow indicates the processing direction, and the inset shows the electron diffraction pattern. (**F**) A transversal grain size distribution from TEM measurements in the top 5-μm-deep layer. (**G**) Variation of average transversal grain (subgrain or cell) sizes along depth from the surface. Error bars represent the standard deviation of grain-size measurements.

Shenyang National Laboratory for Materials Science, Institute of Metal Research, Chinese Academy of Sciences, Shenyang 110016, China.

*These authors contributed equally to this work.
†To whom correspondence should be addressed. E-mail: lu@imr.ac.cn

The top 50-μm-thick surface layer was removed from the as-prepared SMGT Cu sample and cut into a dog-bone tensile specimen. Quasi-static tensile tests of the free-standing GNG foil showed a yield strength of ~660 MPa and a uniform elongation of <2% (Fig. 2A). The measured yield strength, about 10 times that of the CG Cu (63 ± 3 MPa), is consistent quantitatively with that calculated from the Hall-Petch relation based on the measured grain sizes. Such a strong-and-brittle tensile behavior of the GNG foil is analogous to that reported in the literature (*15*). Tensile tests of the SMGT bar samples with a GNG/CG architecture (*14*) showed a yield strength (0.2% offset) of 129 ± 17 MPa (Fig. 2A), twice that of the CG sample. This yield strength increment is reasonably attributed to the strong GNG surface layer and the deformed CG layer. Summing up the estimated strengths of the GNG layer, the deformed CG layer, and the CG core following the rule-of-mixture resulted in a yield strength of about 135 MPa, in good agreement with the measured value.

In contrast to the brittle failure of the free-standing GNG foil, quasi-static tension of the GNG/CG bar samples showed that the GNG surface layer deforms coherently with the CG core in the uniform elongation stage without any surface cracking or delaminating, and the surface roughness is slightly changed (Fig. 2B). After necking, the coherent deformation of the GNG layer and CG core continues, analogous to that of the tensile sample with a monolithic CG structure. No surface cracking or delaminating was detected even in the neck region where the true strain exceeds 100%. The deformed GNG/CG sample surface is much smoother than the deformed CG, both during the uniform deformation and after necking (Fig. 2B).

From more than two dozen tensile tests, we observe a uniform elongation of 31 ± 2% in the GNG/CG sample, which is similar to that of the CG tensile sample with a gauge diameter of 4.5 mm (32 ± 2%). Because the diameter of the deformation-free CG core in the GNG/CG tensile bar is about 4.5 mm, it is believed that the tensile plasticity of the GNG/CG sample is limited by the CG substrate whereas the GNG layer has no detrimental influence on plasticity. Hence, tensile plasticity of the GNG layer is, at least, comparable to that of the CG substrate. Apparently, strain localization in the GNG layer under tension is completely suppressed by the CG substrate with a gradient architecture, of which the tensile behaviors differ fundamentally from that of the free-standing NG samples. The confined GNG layer exhibits a 10-times higher yield strength and a tensile ductility comparable to that of the CG substrate.

For a direct comparison of the tensile plasticity between the GNG and the CG structures, the top 750-μm-thick layer was removed from the SMGT Cu sample and cut into a thin foil tensile specimen, of which one side is of NG structure and the other is CG. Both sides were chemically polished to a roughness in the nanometer regime. Upon tensile loading, plastic deformation occurred uniformly throughout the foil after yielding at about 280 MPa. Necking is seen in three dimensions in the middle of the tensile specimen at a nominal strain of 20% (Fig. 3, A to C). Distinct surface morphologies have developed on the two surfaces.

At a nominal strain of 5%, elongated hollows appeared roughly vertical to the tension direction in the NG surface, submicrometers to micrometers wide and several micrometers long (Fig. 3E). Their depths range from a few to several tens of nanometers. At larger strains, more hollows were formed with larger width. In the neck region (Fig. 3F), hollows are linked, forming a uniform surface morphology with a roughness below 100 nm, without any cracking. In the CG surface, increasing dislocation slip is observed in coarse grains with an increasing strain (Fig. 3H). In the neck region, much larger surface roughness (micrometer-scale) is induced by intensive slip. In addition, small cracks of several micrometers in length were identified at GBs (Fig. 3I), indicating that plastic strain between neighboring grains could not be accommodated by slip and strain localization onsets. Further straining results in

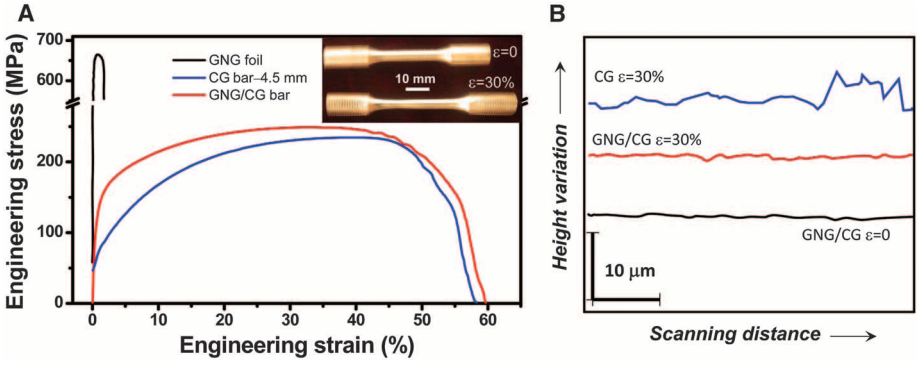

Fig. 2. (**A**) Quasi-static tensile engineering stress-strain curves for the CG Cu bar sample with a gauge diameter of 4.5 mm, the GNG/CG bar sample, and a free-standing GNG foil sample (the top 50-μm-thick layer was removed from the GNG/CG sample, gauge dimensions: 4 mm by 2 mm by 0.05 mm), respectively. Strain rate is 6×10^{-4} s^{-1}. Inset shows the tensile GNG/CG bar samples before and after tension (with a nominal strain of 30%). (**B**) Measured surface height variation profiles in gauge sections of the GNG/CG and the CG bar samples before (both with the same surface roughness) and after tension (with a strain of 30%).

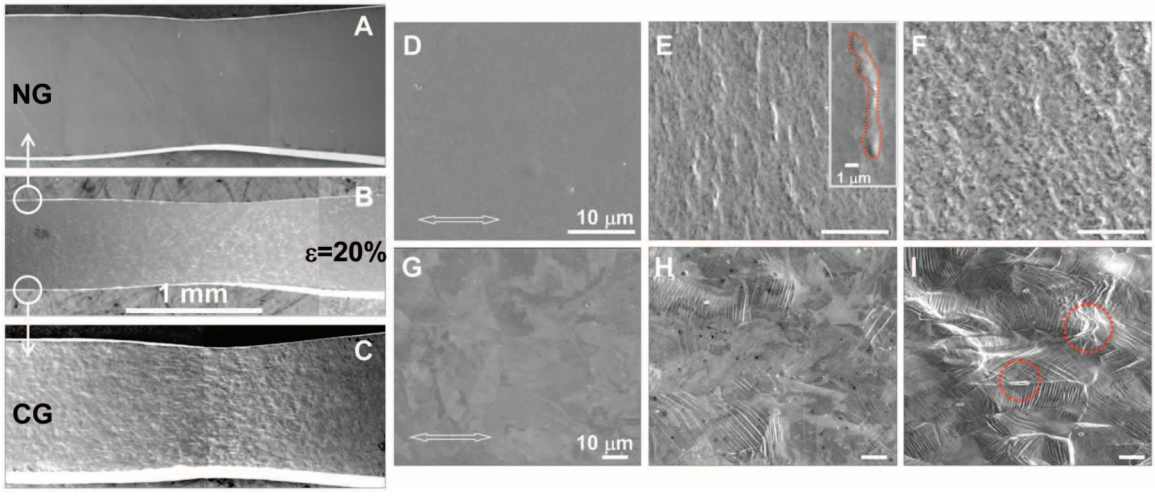

Fig. 3. (**A** to **I**) SEM images of a tensile GNG/CG foil sample (the top 750-μm-thick layer was removed from the as-prepared GNG/CG sample, gauge dimensions: 3 mm by 1 mm by 0.75 mm) with a nominal strain of 20% [(B) side view; (A and C) plan-views of the NG side and the CG side]. Strain rate is 6×10^{-4} s^{-1}. SEM images of both sides of the foil sample with different nominal strains are shown (D), (E), and (F) correspond to the NG side with strains of 0, 5, and 20%; (G), (H), and (I) correspond to the CG side with strains of 0, 5, and 20%, respectively). Inset in (E) is a magnified image of a hollow. Circles in (I) indicate cracks formed at GBs in the CG side. Double-ended arrows indicated tensile directions.

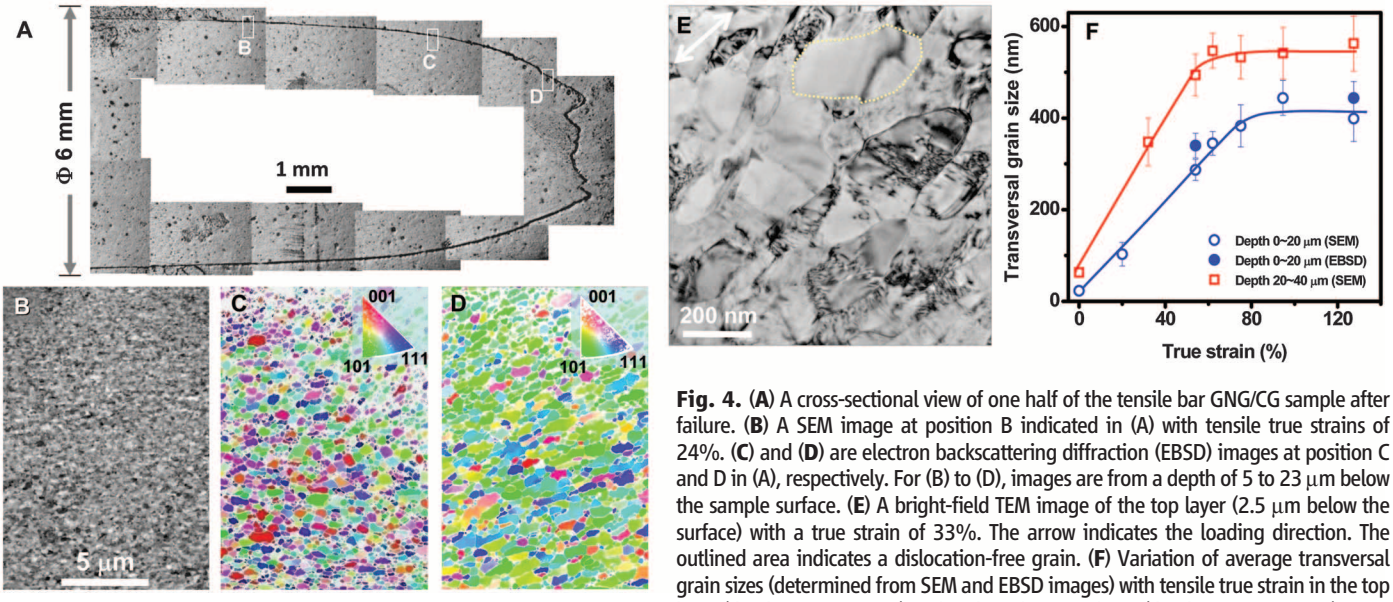

Fig. 4. (**A**) A cross-sectional view of one half of the tensile bar GNG/CG sample after failure. (**B**) A SEM image at position B indicated in (A) with tensile true strains of 24%. (**C**) and (**D**) are electron backscattering diffraction (EBSD) images at position C and D in (A), respectively. For (B) to (D), images are from a depth of 5 to 23 μm below the sample surface. (**E**) A bright-field TEM image of the top layer (2.5 μm below the surface) with a true strain of 33%. The arrow indicates the loading direction. The outlined area indicates a dislocation-free grain. (**F**) Variation of average transversal grain sizes (determined from SEM and EBSD images) with tensile true strain in the top layer (depth of 0 to 20 μm) and in the subsurface layer (depth of 20 to 40 μm). Error bars represent the standard deviation of grain-size measurements.

more cracks that propagate toward the GNG side across the specimen. Plastic deformation is more uniform and better accommodated in the GNG layer than that in the CG, implying that the GNG structure may possess a higher tensile deformability than the CG structure in which cracks form preferentially under the same loading condition.

To reveal the deformation mechanism, we examined microstructures in the GNG layer that underwent different strains in the tensile bar samples after failure (Fig. 4A). The true strain (ε_T) at different positions can be estimated from the gauge diameter (D) by $\varepsilon_T = \ln(D_0^2/D^2)$ (where D_0 is the original gauge diameter). At position B (ε_T = 24%), microstructures in the GNG layer seem coarser than the as-processed state, but details cannot be clearly imaged under scanning electron microscopy (SEM). At ε_T = 54% (Fig. 4C), grain growth is apparent in the GNG layer and roughly equiaxed submicrometer-sized grains with random orientations are developed. At ε_T = 127% (Fig. 4D), grains become even coarser and elongated (roughly along the loading direction, aspect ratio of ~2.0) with a $\{011\}\langle 1\bar{1}2\rangle$ rolling texture.

Cross-sectional TEM observations revealed grain coarsening at a strain of 10%, and a large number of submicrometer-sized grains appeared throughout the GNG layer. At ε_T = 33%, TEM images from different orientations showed that most grains become submicrometer-sized, at which dislocation density is rather low (as in Fig. 4E, some grains are basically dislocation-free as outlined). The area-weighted cumulative grain size distribution in the top GNG layer (fig. S2) and the slightly changed aspect ratio of grains (1.9 to 2.0) indicated a pronounced inhomogeneous grain growth process, i.e., some grains grow preferentially at the expense of others. The same grain growth mechanism was identified in the entire GNG layer at different depths with increasing strains. The observed grain growth in the GNG layer corresponds to a drop in microhardness from about 1.6 ± 0.11 GPa in the top layer before tension to 1.2 ± 0.12 GPa at a true strain of 30%.

The microstructure observations preclude conventional deformation mechanisms in plastic deformation of the GNG layer, such as dislocation slip and diffusion-controlled processes (e.g., Coble creep). The grain growth, which dominates the plastic deformation of the present sample, can be reasonably interpreted as a mechanically driven GB migration process, similar to previous observations in NG metals (*16*–*23*). Mechanically induced grain growth at room temperature has been reported in NG samples under indentation (*16*, *17*), compression (*18*, *19*), and tensile loading (*20*–*23*), and has also been seen in molecular dynamic simulations (*24*). The estimated GB migration velocity in terms of the grain growth data in the GNG layer is of the same order of magnitude as that reported in a NG Al tensile sample (*22*). But the observed GB displacements, as large as micrometers, are much larger than the reported results (up to submicrometers). Although such a large GB displacement at room temperature is difficult to explain with existing models (*25*, *26*), it could be understood as the result of an energy release due to substantial defect annihilation in the nanostructures, which can accommodate the large plastic strains.

With an increasing true strain (or true stress, which scales with true strain), the average grain size increases substantially and tends to saturation when ε_T > 80% (Fig. 4F). It implies that the dominant plastic deformation mechanism shifts from the mechanically driven GB migration to conventional dislocation slip when grain sizes are large enough, as verified by the observed rolling texture (Fig. 4D). In the top surface layer, grain growth rates are lower, with a smaller saturated grain size (~400 nm) than that in the subsurface layer, which might be attributed to the varied grain morphology and GB structures along depth. A large fraction of GBs in the top GNG layer were derived from twin boundaries (TBs) induced by high strain rates, whereas in the subsurface layer with much lower strain rates, most GBs are conventional high-angle boundaries derived from dislocation structures (*27*). Hence, GBs in the subsurface layer possess a higher excess energy than those TB-like boundaries in the top layer, as verified by diffusivity measurements (*28*).

Our study shows that NG metals are not only strong but also intrinsically ductile as long as strain localization is effectively suppressed. The extraordinary plasticity of the NG structures originates from a deformation mechanism with concomitant mechanically driven growth of nano-sized grains. The intrinsic mechanical properties of NG materials and the GNG/CG architecture provide an approach for enhancing strength-ductility synergy of materials and offer the potential for using gradient NG layers as advanced coatings of bulk materials.

References and Notes

1. H. Gleiter, *Prog. Mater. Sci.* **33**, 223 (1989).
2. J. Chen, L. Lu, K. Lu, *Scr. Mater.* **54**, 1913 (2006).
3. M. A. Meyers, A. Mishra, D. J. Benson, *Prog. Mater. Sci.* **51**, 427 (2006).
4. K. S. Kumar, S. Suresh, M. F. Chisholm, J. A. Horton, P. Wang, *Acta Mater.* **51**, 387 (2003).
5. A. Hasnaoui, H. Van Swygenhoven, P. M. Derlet, *Science* **300**, 1550 (2003).
6. Y. M. Wang, E. Ma, M. W. Chen, *Appl. Phys. Lett.* **80**, 2395 (2002).
7. L. Lu, M. L. Sui, K. Lu, *Science* **287**, 1463 (2000).
8. Y. Xiang, T. Li, Z. Suo, J. Vlassak, *Appl. Phys. Lett.* **87**, 161910 (2005).
9. N. Lu, X. Wang, Z. Suo, J. Vlassak, *J. Mater. Res.* **24**, 379 (2009).
10. S. Suresh, *Science* **292**, 2447 (2001).
11. K. Lu, J. Lu, *J. Mater. Sci. Technol.* **15**, 193 (1999).

12. K. Lu, J. Lu, *Mater. Sci. Eng. A* **375-377**, 38 (2004).
13. W. L. Li, N. R. Tao, K. Lu, *Scr. Mater.* **59**, 546 (2008).
14. Materials and methods are available as supporting material on *Science* Online.
15. Y. M. Wang *et al.*, *Scr. Mater.* **48**, 1581 (2003).
16. K. Zhang, J. R. Weertman, J. A. Eastman, *Appl. Phys. Lett.* **85**, 5197 (2004).
17. M. Jin, A. M. Minor, E. A. Stach, J. W. Morris Jr., *Acta Mater.* **52**, 5381 (2004).
18. D. Pan, S. Kuwano, T. Fujita, M. W. Chen, *Nano Lett.* **7**, 2108 (2007).
19. S. Brandstetter, K. Zhang, A. Escuadro, J. Weertman, H. Van Swygenhoven, *Scr. Mater.* **58**, 61 (2008).
20. D. S. Gianola *et al.*, *Acta Mater.* **54**, 2253 (2006).
21. T. J. Rupert, D. S. Gianola, Y. Gan, K. J. Hemker, *Science* **326**, 1686 (2009).
22. M. Legros, D. S. Gianola, K. J. Hemker, *Acta Mater.* **56**, 3380 (2008).
23. G. J. Fan, L. F. Fu, H. Choo, P. K. Liaw, N. D. Browning, *Acta Mater.* **54**, 4781 (2006).
24. J. Schiotz, *Mater. Sci. Eng. A* **375-377**, 975 (2004).
25. J. W. Cahn, Y. Mishin, A. Suzuki, *Acta Mater.* **54**, 4953 (2006).
26. J. C. M. Li, *Phys. Rev. Lett.* **96**, 215506 (2006).
27. K. Wang, N. R. Tao, G. Liu, J. Lu, K. Lu, *Acta Mater.* **54**, 5281 (2006).
28. Z. B. Wang, K. Lu, G. Wilde, S. V. Divinski, *Acta Mater.* **58**, 2376 (2010).

29. We thank X. Si for assistance in sample preparation and J. Tan for assistance in EBSD experiments. We are grateful for financial support of the Ministry of Science and Technology of China (grant 2005CB623604, 2010DFB54010), the National Natural Science Foundation (grants 50890171, 50971122), and the Danish–Chinese Center for Nanometals (grant 50911130230).

Supporting Online Material

www.sciencemag.org/cgi/content/full/science.1200177/DC1
Materials and Methods
Figs. S1 and S2

8 November 2010; accepted 7 February 2011
Published online 17 February 2011;
10.1126/science.1200177

Self-Recognition Among Different Polyprotic Macroions During Assembly Processes in Dilute Solution

Tianbo Liu,[1]* Melissa L. K. Langston,[1] Dong Li,[1] Joseph M. Pigga,[1] Céline Pichon,[1] Ana Maria Todea,[2] Achim Müller[2]*

We report a self-recognition phenomenon based on an assembly process in a homogeneous dilute aqueous solution of two nano-scaled, spherical polyprotic metal oxide–based macroions (neutral species in crystals), also called Keplerates of the type $[(linker)_{30}(pentagon)_{12}] \equiv [\{M(H_2O)\}_{30}\{(Mo)Mo_5\}_{12}]$ where M is Fe^{III} or Cr^{III}. Upon deprotonation of the neutral species, the resulting macroions assemble into hollow "blackberry"-type structures through very slow homogeneous dimer-oligomerization processes. Although the geometrical surface structures of the two macroions are practically identical, mixtures of these form homogeneous superstructures, rather than mixed species. The phase separation is based on the difference in macroionic charge densities present during the slow homogeneous dimer or oligomer formation. The surface water ligands' residence times of Cr^{III} and Fe^{III} differ markedly and lead to very different interfacial water mobilities between the Keplerates.

Molecules in solution can self-assemble into larger structures through weak interactions (*1*, *2*). For example, lipid molecules of the same type can assemble in water into larger micelles (*2*). By contrast, shape and polarity complementarity of different molecules can direct self-assembly through molecular recognition (*1*, *2*). One way to explore interaction-based processes in the context of self-recognition (*3*) is to examine solutions with mixed species that do not exhibit complementary properties to determine whether self-assembly leads to phase separation or creates structures containing different species. To this end, we studied solutions containing two different hydrophilic, porous, metal oxide–based molecular clusters with identical surface structures that bear multiple metal cations (Lewis acid sites) with influential coordinated water ligands. These 2.5-nm-size clusters of the Keplerate type (Fig. 1A) are intermediate in size between simple ions and colloids (*4*–*11*), get deprotonated in aqueous solution, and have a distinctive solution behavior: They (but also other giant inorganic ions) tend to spontaneously and reversibly assemble into stable, uniform, single-layered, shell-like "blackberry" structures instead of existing as discrete ions in dilute solution (*12*–*18*). The formation of these structures is mediated by counterion attractions and hydrogen bonding, as opposed to van der Waals forces, hydrophobic interactions, or chemical reactions (*15*, *18*), which in the present case leads to a phase separation, i.e., two superstructures with no interference or crossover (*3*).

We examined aqueous solutions containing the two spherical polyprotic clusters of the type $[(linker)_{30}(pentagon)_{12}] \equiv [\{M(H_2O)\}_{30}\{(Mo)Mo_5\}_{12}]$, where M is Fe^{III} or Cr^{III} (*4*, *5*) (below abbreviated as $\{Mo_{72}Fe_{30}\}$ and $\{Mo_{72}Cr_{30}\}$; structural details are shown in Fig. 1, and the chemical formulae in Materials and Methods). The clusters have, according to the properties of the 30 characteristic and active $M(H_2O)$ groups coordinated to the non-Mo atoms, extremely different mobilities of their surface hydration layers as well as degrees of deprotonation (*13*–*15*). Specifically, the water ligands (weak Brønsted acids) release protons, i.e., about seven for $\{Mo_{72}Fe_{30}\}$ and about five for $\{Mo_{72}Cr_{30}\}$ in aqueous solutions, which leads to a comparably smaller surface charge of the latter (*15*). Correspondingly, the degree of deprotonation of the clusters changes with the pH. One result is that upon, for example, addition of acid, the size of the blackberry increases monotonically with decreasing pH, i.e., with decreasing charge density on the macroions (*13*–*15*). At pH ~3.5 to 4.5, for instance, the superstructures formed in aqueous solution of $\{Mo_{72}Cr_{30}\}$ have an average hydrodynamic radius (R_h) of ~60 to 80 nm [measured by dynamic light scattering (DLS) and transmission electron microscopy], which is larger than that of the corresponding $\{Mo_{72}Fe_{30}\}$ blackberries (~20 to 30 nm) (*13*–*15*). At low pH (~2.5), both types of clusters stay as discrete (protonated) neutral molecules in aqueous solution without showing the assembly phenomenon.

We studied the mixed aqueous solutions of the $\{Mo_{72}Cr_{30}\}$- and $\{Mo_{72}Fe_{30}\}$-type Keplerates to determine whether they form homogeneous or heterogeneous blackberry-type structures (Fig. 1C). Aqueous solutions containing both types of macroanion (1:1 mass ratio, up to 0.5 mg/ml each) were prepared and then maintained at 30° or 40°C; the assembly processes start slowly and last for several weeks. The resulting two separated modes in the CONTIN analysis (*19*) of the DLS study indicated the presence of two differently sized large species (Fig. 1C and red curve in Fig. 2A). The two peaks correspond, within the error limit of the CONTIN analysis, to those of the individual solutions containing either $\{Mo_{72}Cr_{30}\}$ or $\{Mo_{72}Fe_{30}\}$ at the same pH value (Fig. 2A).

We obtained further evidence for self-recognition in the assembly process by separating the two formed large "final products" in the mixed solutions with a series of filter membranes of different pore sizes, starting with the largest ones [for details, see Materials and Methods (*20*)]. A CONTIN analysis of fraction A (*20*) showed a peak at an R_h of ~60 to 80 nm (Fig. 2B), consistent with the peak of the pure $\{Mo_{72}Cr_{30}\}$ solution. These larger assemblies have, by element analysis, a Cr:Fe mass ratio of ~1:0.02, demonstrating that they are formed almost entirely from $\{Mo_{72}Cr_{30}\}$. The CONTIN analysis of fraction B (*20*) showed a peak at an R_h of ~25 nm (Fig. 2B), i.e., almost identical to that of the pure $\{Mo_{72}Fe_{30}\}$ solution. However, because of the incomplete membrane separation, these smaller assemblies have, by element analysis, a relative

[1]Department of Chemistry, Lehigh University, Bethlehem, PA 18015, USA. [2]Fakultät für Chemie, Universität Bielefeld, D-33501 Bielefeld, Germany.

*To whom correspondence should be addressed. E-mail: liu@lehigh.edu (T.L.); a.mueller@uni-bielefeld.de (A.M.)